

**Efficient operator method for modeling mode mixing in misaligned optical cavities**W. J. Hughes <sup>1,\*</sup>, T. H. Doherty <sup>1</sup>, J. A. Blackmore <sup>1</sup>, P. Horak <sup>2</sup> and J. F. Goodwin <sup>1,†</sup><sup>1</sup>*Department of Physics, University of Oxford, Clarendon Laboratory, Parks Road, Oxford OX1 3PU, United Kingdom*<sup>2</sup>*Optoelectronics Research Centre, University of Southampton, Southampton SO17 1BJ, United Kingdom*

(Received 16 June 2023; revised 13 November 2023; accepted 20 December 2023; published 31 January 2024)

The transverse field structure and diffraction loss of the resonant modes of Fabry-Pérot optical cavities are acutely sensitive to the alignment and shape of the mirror substrates. We develop extensions to the mode-mixing method applicable to arbitrary mirror shapes, which both facilitate fast calculation of the modes of cavities with transversely misaligned mirrors and enable the determination and transformation of the geometric properties of these modes. We show how these methods extend previous capabilities by including the practically motivated case of transverse mirror misalignment, presenting the ability to study the rich and complex structure of the resonant modes.

DOI: [10.1103/PhysRevA.109.013524](https://doi.org/10.1103/PhysRevA.109.013524)**I. INTRODUCTION**

The majority of Fabry-Pérot optical cavities have mirrors with sufficiently constant curvature to be described well by standard resonator theory [1]. However, there are applications of cavities with nonspherical mirrors for which standard theory is not suitable. As the first example, the desire to realize stronger light-matter coupling, whether to increase the rate of single-photon sources [2] or to observe light-matter hybridization [3], has led to the use of microcavities [4]; specialist fabrication techniques, such as laser ablation [5] or chemical etching [6], that can manufacture the requisite highly curved micromirrors typically produce mirrors that are not perfectly spherical [7–9]. Second, in cavity optomechanics, the advantages conferred by low-mass mirrors encourage lightweight designs with limited diameter [10,11]. Finally, cavities with nonspherical mirrors offer useful optical capabilities, for example, flexibility to tailor the optical mode [12,13], control the number of resonances [14,15], or utilize polarization properties [16].

As such experiments mature towards applications, it is important to calculate the required precision for transverse mirror alignment. For the spherical mirror case, there are simple methods for calculating the resonant modes under transverse mirror misalignment [5,17], but these do not necessarily apply well to cavity mirrors with alternative shapes. This paper details extensions to the mode-mixing method [18], allowing for certain mirror shapes to be encoded without numerical integration and for arbitrary mirror shapes to

be transversely misaligned without further integration. These advances greatly reduce, and potentially eliminate, the computation devoted to numerical integration, yielding a method that allows for the impact of transverse misalignment in cavities with deformed mirrors to be investigated thoroughly.

First, we present an intuitive geometric optics approach to predicting the modes of cavities with misaligned and nonspherical mirrors. We then overview the existing mode-mixing method before detailing extensions that greatly simplify the calculations required to model particular mirror shapes and to include transverse mirror misalignment. We then discuss geometric transformations of cavity modes that can be used to interpret calculation outputs. Finally, we compare these methods to existing techniques, demonstrating good agreement with published results for Gaussian-shaped mirrors in aligned configurations while additionally permitting the easy exploration of the impact of mirror misalignment. In another work [19] we use the methods developed in this paper to examine the behavior of cavities with spherical and Gaussian mirrors under transverse misalignment.

**II. GEOMETRIC ANALYSIS OF MODE DEFORMATION**

Before introducing our approach to mode-mixing calculations in cavities with deformed mirrors and residual misalignment, we review the problem with a simple geometric optics picture that serves to highlight the physics of misaligned cavities in a more intuitive, albeit less complete, manner. In this “geometric” approach to determining the cavity modes, the propagation axis of the mode must intersect both mirrors normal to their surface so that the mode is perfectly retroreflected. The phase curvature of the cavity mode at the intersection with each mirror is then matched to the local curvature of the mirror about the intersection point, as described in [20]. This condition determines the positions and sizes of the transverse waists of the cavity mode in both transverse directions.

\*william.hughes@physics.ox.ac.uk

†joseph.goodwin@physics.ox.ac.uk

Published by the American Physical Society under the terms of the [Creative Commons Attribution 4.0 International license](https://creativecommons.org/licenses/by/4.0/). Further distribution of this work must maintain attribution to the author(s) and the published article’s title, journal citation, and DOI.

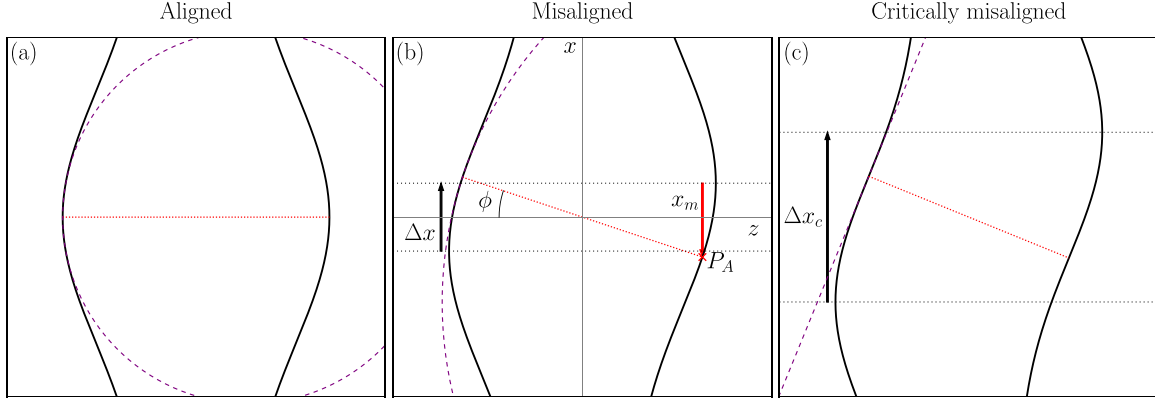


FIG. 1. Schematic of cavity mode geometry in misaligned optical cavities, shown for the example case of Gaussian-shaped mirrors. (a) Perfect, symmetric alignment of the two mirror profiles (black solid lines). The cavity mode axis (red dotted line) is aligned to both mirror axes. The radius of curvature of the phase fronts on the mirror matches the central curvature (purple dashed line). (b) Small transverse misalignment  $\Delta x$  of the mirrors. The mode tilts at an angle  $\phi$  to the mirror axes (horizontal black dotted lines), intersecting the mirror at point  $P_A$ , which is at displacement  $x_m$  from the center of the mirror. The curvature at the intersection point (purple dashed line) is different from the center of the mirror. (c) Mode instability for large mirror displacement. At sufficiently large misalignment, the cavity mode axis may tilt at such an angle that neither mirror surface is concave at the mode intersection point and no stable mode is predicted.

We consider the features predicted when applying this approach to Fabry-Pérot cavities whose mirrors are transversely misaligned such that they are no longer coaxial. For general mirror shapes, the modes predicted can have general astigmatism, with an intensity profile that twists along the cavity axis, requiring an involved mathematical treatment [21]. However, for simplicity, we will illustrate the approach using spherically symmetric Gaussian-shaped mirrors as a specific example, as depicted in Fig. 1. Gaussian mirrors have a depth profile

$$f_G(x, y) = D \left[ 1 - \exp\left(-\frac{x^2 + y^2}{w_e^2}\right) \right], \quad (1)$$

where  $x$  and  $y$  are Cartesian coordinates transverse to the mirror axis,  $D$  is the depth of the mirror, and  $w_e$  is the  $1/e$  waist. These parameters define the central radius of curvature  $R_c = w_e^2/2D$ . By convention, the depth profile is zero at the center of the depression and positive as the concave mirror protrudes towards the center of the cavity.

Figure 1(a) shows the case of perfect alignment. The predicted mode lies along both (collinear) mirror axes, with the wave-front curvature at each mirror matching the center radius of curvature  $R_c$ . The corresponding fundamental Gaussian mode can be calculated using standard spherical cavity theory [22]. Note that this yields a poor approximation of the fundamental mode if the mirror shape deviates significantly from spherical over the scale of the mode.

If the cavity mirrors are transversely misaligned, as shown Fig. 1(b), the cavity mode axis must tilt so that it can intersect both mirrors at normal incidence. This means that the local radius of curvature of the mirrors at the position of intersection may differ from  $R_c$ , producing a mode with a different waist compared to a cavity with aligned mirrors. Moreover, the local radius of curvature may differ in the two transverse directions, making the cavity mode an elliptical Gaussian beam.

To analyze these effects quantitatively, we construct a coordinate system in which the centers of the two mirrors, labeled A and B, are placed at coordinates  $z_A = L/2$  and  $z_B = -L/2$ ,

respectively, along the  $z$  axis, where  $L = z_A - z_B$  is the cavity length and the  $z$  axis is the cavity axis in the aligned configuration. The misalignment direction is taken to define the  $x$  axis and thus the two mirrors are displaced by  $\pm\Delta x/2$  in the  $x$  direction, respectively, as shown in Fig. 1(b). The point  $P_A = (x_{P_A}, y_{P_A}, z_{P_A})$  where the cavity axis intersects mirror A can be calculated from the requirement that the cavity axis is locally orthogonal to the mirror; with  $x_m = x_{P_A} - \Delta x/2$  defined as the distance of point  $P_A$  from the center of the mirror, the solution satisfies

$$\frac{\Delta x}{2} = 2D \frac{x_m}{w_e^2} e^{-x_m^2/w_e^2} \left( \frac{L}{2} + D(-1 + e^{-x_m^2/w_e^2}) \right) - x_m, \quad (2)$$

which can be solved numerically for  $x_m$  and then used to calculate the coordinates of  $P_A$ .

With the mode axis determined, the properties of the cavity mode can be simply derived. The effective length of the cavity mode between the intersections with the mirror is

$$L_{\text{eff}} = 2\sqrt{x_{P_A}^2 + z_{P_A}^2}. \quad (3)$$

The radius of curvature of the mirror at  $P_A$  in the  $x$  direction is

$$R_x = \frac{[1 + f_G'(x_m, 0)]^{3/2}}{f_G''(x_m, 0)}, \quad (4a)$$

$$f_G'(x_m, 0) = 2D \frac{x_m}{w_e^2} e^{-x_m^2/w_e^2}, \quad (4b)$$

$$f_G''(x_m, 0) = D \frac{2}{w_e^2} e^{-x_m^2/w_e^2} \left[ 1 - \left( \frac{\sqrt{2}x}{w_e} \right)^2 \right], \quad (4c)$$

where  $f_G'(x, y)$  and  $f_G''(x, y)$  are first and second derivatives of the mirror profile  $f_G(x, y)$  [Eq. (1)] with respect to  $x$ . The radius of curvature in the  $y$  direction is

$$R_y = R_c e^{x_m^2/w_e^2} \cos \phi + x_m \sin \phi, \quad (5a)$$

$$\sin \phi = \frac{x_{P_A}}{\sqrt{x_{P_A}^2 + z_{P_A}^2}}, \quad (5b)$$

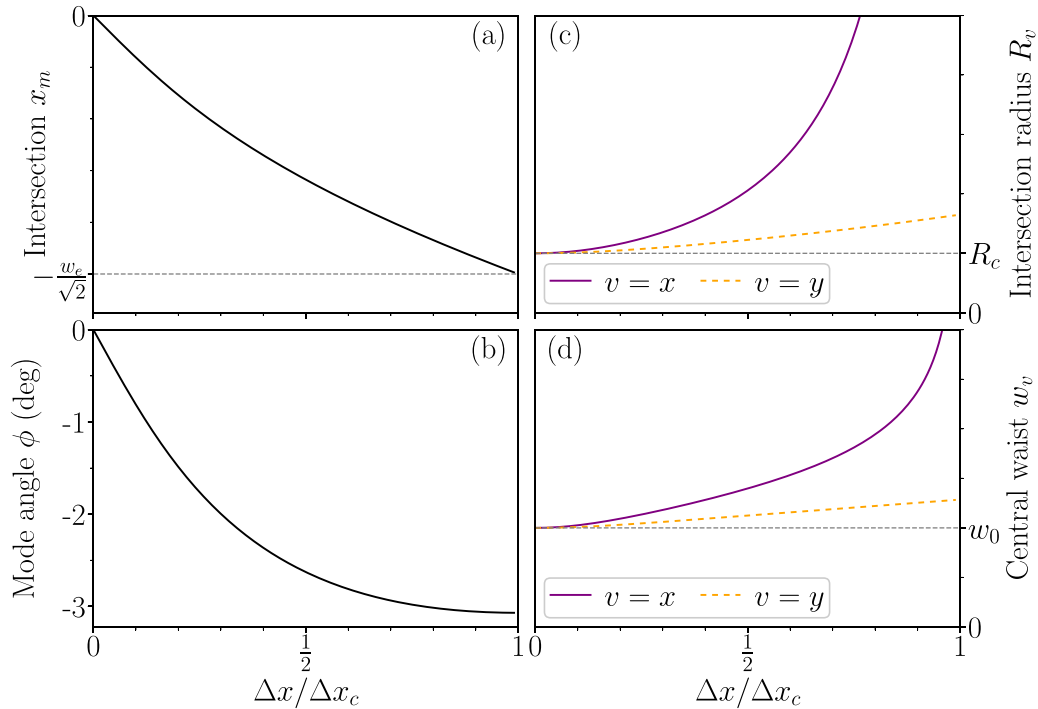


FIG. 2. Case study of the predicted mode in cavities with Gaussian-shaped mirrors under transverse misalignment, generated for a cavity with  $L = 500 \mu\text{m}$ ,  $R_c = 400 \mu\text{m}$ , and  $w_e = 50 \mu\text{m}$ , with interrogation wavelength 866 nm: (a) intersection coordinate relative to the center of the mirror, (b) tilt angle  $\phi$ , (c) local radii of curvature at the mode intersection  $R_v$  for  $v \in \{x, y\}$ , and (d) predicted central waists in the  $x$  and  $y$  directions.

where  $\phi$  is the angle of the cavity mode axis with respect to the  $z$  axis. The central waists are

$$w_{0,v} = \sqrt{\frac{\lambda L_{\text{eff}}}{2\pi} \left( \frac{2R_v}{L_{\text{eff}}} - 1 \right)}, \quad (6)$$

where  $v \in \{x, y\}$  specifies the transverse coordinate.<sup>1</sup>

For large mirror misalignments, the mode axis may intersect the mirror sufficiently far from the central depression that the local profile is not concave, as shown Fig. 1(c). In this case the cavity is not able to stably confine a mode. For Gaussian mirrors, this occurs for misalignments  $\Delta x$  exceeding  $\Delta x_c$  at which  $x_m = \pm w_e/\sqrt{2}$ .

A numerical case study applying this procedure to a cavity with Gaussian-shaped mirrors is presented in Fig. 2. This shows that, as the mirrors are misaligned, the mode angle and the position of intersection on the mirror deviate increasingly from their aligned values. The off-axis intersection means that the local radius of curvature at the intersection points increases in both the  $x$  and  $y$  directions. However, the change is much larger in the  $x$  direction. At the critical misalignment  $\Delta x_c$  ( $44.0 \mu\text{m}$  for the parameters of Fig. 2), the mode intersection point is sufficiently far from the center of the mirror that the local mirror surface is not concave. This means that the cavity is unstable, and one would expect to observe a severe drop in finesse.

This geometric analysis of the fundamental mode limits itself to cavity modes with quadratic wave-front curvature and

therefore does not take into account the mirror shape beyond its local gradient and radius of curvature. Though the mirror surface can always be approximated as parabolic close enough to the intersection point, the geometric analysis becomes unsuitable when the mode is sufficiently wide on the mirror that higher-order components of the profile become significant. To calculate cavity modes for cases where the mirror profile is not perfectly parabolic about the mode intersection points, we must use a framework with the flexibility to model cavity modes with more general wave-front curvature profiles.

### III. EXTENDED MODE-MIXING METHOD

#### A. Mode-mixing introduction

A variety of methods have been developed to calculate the modes of cavities with nonspherical mirror profiles. Besides mode mixing, these include iterative diffraction integral techniques [23,24], discrete linear canonical transforms [25], or discrete Hankel transforms (for the case of spherical symmetry) [26]. This section discusses the mode-mixing method. It should be noted all methods above apply to linear optical resonators. These require modification to study nonlinear optical phenomena (see [27] for an example iterative method), which are common applications of microcavity systems [28–30].

The mode-mixing method [18] finds the stable modes of cavities with deformed mirrors by expressing propagating fields as linear superpositions of Gaussian modes. This method has been applied to microcavities with nonspherical mirrors, finding sporadic, severe drops in cavity finesse at particular cavity lengths due to resonant mixing of the basis modes [31,32]. Alternatively, mode mixing can be used

<sup>1</sup>The principal axes of the mode will be in the  $x$  and  $y$  directions because the transverse misalignment is  $x$  directed.

to understand diffraction loss [26,33], increase coupling of cavity fields to single emitters [34–36], introduce coupling between optical resonators [37], or tailor cavity modes for desired applications [12,13]. Standard mode-mixing theory is introduced in this section, before extensions to facilitate the calculations, particularly in the context of misaligned cavities, are presented.

In principle, a propagating electric field satisfies Maxwell's equations. Typically, these equations are simplified by employing the paraxial approximation, which assumes that the propagating field is beamlike and directed at small angles to the nominal  $z$  axis. Under these assumptions (see [38], with which the notation presented is consistent), the electric field can be described via a scalar function  $u^\pm$  through

$$\mathbf{E}(x, y, z, t) = \epsilon u^\pm(x, y, z) \exp(\mp ikz) \exp(i\omega t), \quad (7)$$

where  $\omega$  is the angular frequency,  $k = \omega/c$  is the wave vector,  $\epsilon$  is the constant linear polarization of the field, which must lie in a plane perpendicular to the  $z$  axis, and  $\pm$  denotes propagation towards positive or negative  $z$ , respectively. The function  $u^\pm$  satisfies the paraxial wave equation

$$\frac{\partial}{\partial z} u^\pm(x, y, z) = \mp \frac{i}{2k} \left( \frac{\partial^2}{\partial x^2} + \frac{\partial^2}{\partial y^2} \right) u^\pm(x, y, z). \quad (8)$$

In the mode-mixing formalism, an electromagnetic field propagating along the  $z$  axis according to Eq. (8) is expressed as a linear superposition of modes  $u_s^\pm(x, y, z)$ , which themselves satisfy the paraxial equation, where  $s$  is an index over all the modes in the basis. An optical element is encoded as a matrix whose elements are scattering amplitudes from ingoing modes in the ingoing basis to outgoing modes in the outgoing basis. In the case of a concave mirror illuminated at normal incidence, the input and output basis states counterpropagate and the mirror profile imprints a differing phase across the wave front due to the variation in propagation distance to and from the mirror. The components of a mirror matrix  $A$  ( $B$ ) at positive (negative)  $z$  coordinate may be written

$$A_{s,t} = \int_{S_A} u_s^{-*}(x, y, z_A) \exp[2ikf_A(x, y)] u_t^+(x, y, z_A) dS, \quad (9a)$$

$$B_{s,t} = \int_{S_B} u_s^{+*}(x, y, z_B) \exp[2ikf_B(x, y)] u_t^-(x, y, z_B) dS, \quad (9b)$$

where  $k$  is the wave vector of the light,  $z_A$  ( $z_B$ ) is the axial coordinate of the center of the depression of mirror A (B),  $f_A$  ( $f_B$ ) is the surface profile of mirror A (B) (with the convention that a positive profile points towards the cavity center for both mirrors), and  $S_A$  ( $S_B$ ) is the surface region of mirror A (B). The surface integrals are each performed in a single transverse plane at the axial coordinate for which  $f_A$  is zero. A schematic diagram illustrating how a mirror transfers amplitude from the input basis to the output basis is shown in Fig. 3. Cavity eigenmodes are specific linear superpositions of basis states that are preserved after one round-trip of a cavity.

In this paper, all calculations are performed in the computational basis, which expresses the cavity function  $u^\pm(x, y, z)$

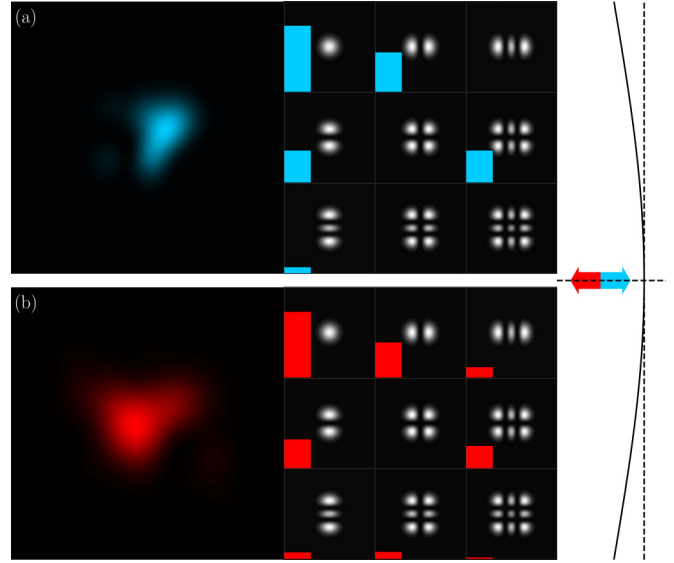


FIG. 3. Diagram of the mode mixing introduced by reflection from a mirror. (a) An arbitrary incoming beam (blue) is expressed as a linear superposition of incoming basis states (here the basis states for  $n_x$  and  $n_y$ , up to 2 are shown). The amplitudes of the coefficients are depicted by the height of the bars adjacent to the corresponding basis states. The mirror (black solid concave profile), shown as having a Gaussian profile, imprints a phase front on the input beam and reverses its direction. (b) The output beam (red) is expressed as a linear superposition of basis states in the outgoing basis. The intensity patterns of the input and output beams are plotted in the transverse plane in which both bases have their central waist. The beams presented are intentionally irregular to highlight the general applicability of the mirror matrix.

as a linear superposition of the Hermite-Gaussian modes

$$u_{n_x, n_y}^{(\pm)}(x, y, z) = a(z) H_{n_x} \left( \frac{\sqrt{2}x}{w(z)} \right) H_{n_y} \left( \frac{\sqrt{2}y}{w(z)} \right) \times \exp \left( -\frac{x^2 + y^2}{w(z)^2} \right) \exp \left( \mp ik \frac{x^2 + y^2}{2R_u(z)} \right) \times \exp[\pm i(n_x + n_y + 1)\Psi_G], \quad (10)$$

where

$$a(z) = \frac{1}{w(z)} \sqrt{\frac{2}{\pi} \frac{1}{2^{n_x + n_y} n_x! n_y!}}, \quad w(z) = w_0 \sqrt{1 + \left( \frac{z}{z_0} \right)^2},$$

$$z_0 = \frac{\pi w_0^2}{\lambda}, \quad R_u(z) = z \left[ 1 + \left( \frac{z_0}{z} \right)^2 \right],$$

$$\Psi_G(z) = \arctan \left( \frac{z}{z_0} \right), \quad (11)$$

where the wavelength  $\lambda = 2\pi/k$ ;  $H_i$  are the Hermite polynomials with  $n_x, n_y \in \mathbb{N}$ , with the  $x$  and  $y$  transverse indices; and  $z_0$  is the Rayleigh range of the beam. This basis is complete and orthonormal for each transverse plane separately. A cavity function expressed as a linear superposition of these basis modes retains its mode coefficients during propagation, as the propagation of the field is encoded in the  $z$  dependence of the basis functions themselves.

The round-trip matrix can be calculated from the two mirror matrices, accounting for the round-trip phase accumulated during propagation:

$$M = BAe^{-2ikL}. \quad (12)$$

A mode  $|\Psi_i\rangle$  supported by the cavity is an eigenmode of the round-trip matrix  $M$  and has corresponding eigenvalue  $\gamma_i$  from the eigenmode equation

$$M|\Psi_i\rangle = \gamma_i|\Psi_i\rangle. \quad (13)$$

The complex  $\gamma_i$  has both phase and amplitude. The complex phase is the round-trip phase (modulo  $2\pi$ ) accrued by  $|\Psi_i\rangle$ , which is zero on resonance. For typical applications where the length can be tuned freely to match a given resonance, the amplitude is more pertinent as it leads directly to the round-trip loss  $\mathcal{L}_{RT} = 1 - |\gamma_i|^2$ .

The eigenmodes of cavities with deformed mirrors can be determined by calculating elements of mirror matrices  $A$  and  $B$  through integration of Eq. (9). A sensible approach to calculating the eigenmodes of cavities with transverse misalignment would therefore appear to be to calculate the geometrically expected mode as a function of misalignment using the theory of Sec. II and use this mode to define the basis of the mode-mixing calculation. Using this approach, the basis of the mode-mixing calculation is always chosen to suit the geometric model and therefore it should be easier to faithfully capture the cavity eigenmodes with a relatively limited basis size.

However, performing calculations this way uses a different basis for every misalignment and cavity length. Therefore, all of the matrix elements are calculated for each cavity configuration separately. Furthermore, the basis states themselves would generally have a more complicated form than those in Eq. (10). The alternative approach detailed in this paper uses matrix operations to misalign the mirrors without changing the calculation basis, thus removing the need to explicitly encode the mirror profiles for every misalignment. Once the cavity eigenmodes have been calculated in the computational basis, they can be simply expressed in other bases for the purposes of analysis, as will be exemplified in Sec. IV.

Finally, it should be noted that the method of this paper uses the paraxial approximation, which assumes that the modes propagate at small angles to the optical axis. Under this assumption, the mode polarization [denoted by  $\epsilon$  in Eq. (7)] is transverse to the optical axis and constant. Corrections to this approximation [39] introduce longitudinally polarized components and modify the mode profile [40,41]. These corrections are typically small for all but the most extreme Fabry-Pérot cavity designs [42]; however, they can have notable effects by mixing modes that are degenerate in the paraxial theory. For example, the local ellipticity discussed in Sec. II results in a birefringent splitting

$$\Delta\nu = \frac{c}{2L} \frac{1}{2\pi k} \frac{R_x - R_y}{R_x R_y}, \quad (14)$$

where  $c$  is the speed of light, which will be observable if the splitting exceeds the cavity linewidth [8]. Additional nonparaxial corrections include polarization-dependent penetration of Bragg reflectors [43] and coupling between the

optical spin and orbital angular momenta [44] and are discussed in detail in [45,46].

## B. Replacing coordinates with operators

The long-appreciated similarities between the Hermite-Gaussian modes and simple-harmonic-oscillator wave functions [47,48] inspire the writing of transverse coordinates  $x$  ( $y$ ) and transverse derivatives  $\partial/\partial x$  ( $\partial/\partial y$ ) in terms of the ladder operators  $a_x$  ( $a_y$ ), where  $a_x$  ( $a_y$ ) reduces the  $n_x$  ( $n_y$ ) index of the Hermite-Gaussian mode by 1. Such operator methods have already been used to determine the eigenmodes of optical cavities under particular circumstances [21,27,45,49]. According to the conventions of the present analysis, the operators for  $x$  and  $\partial/\partial x$  in a given transverse plane are

$$x^{(\pm)}(z) = U_G^{(\pm)}(z) \frac{1}{2} w(z) (a_x + a_x^\dagger) U_G^{(\pm)}(z), \quad (15a)$$

$$\frac{\partial}{\partial x} = \frac{1}{w_0} (a_x - a_x^\dagger), \quad (15b)$$

$$(U_G)^{(\pm)}(z)_{n'_x, n'_y, n_x, n_y} = e^{\pm i\Psi_G(z)(n_x + n_y + 1)} \delta_{n'_x, n_x} \delta_{n'_y, n_y}, \quad (15c)$$

where  $n_x$  and  $n_y$  ( $n'_x$  and  $n'_y$ ) are the  $x$  and  $y$  indices of the input (output) modes of the matrix, respectively. While the  $\partial/\partial x$  operator does not depend on propagation direction and is constant across all transverse planes, the matrix elements of  $x$  depend upon the  $z$  coordinate and the propagation direction. The equivalent relations hold for  $y$  and  $\partial/\partial y$ , with  $a_y$  ( $a_y^\dagger$ ) replacing  $a_x$  ( $a_x^\dagger$ ). The derivations are detailed in Appendix A.

A mirror imprints a phase front onto and reflects the incoming mode [as expressed in Eq. (9)]. To construct mirror matrices in an operator-based approach, it is conceptually simpler to consider this process sequentially (taking mirror A as the example case). First, the phase front  $\exp(2ikf_A)$  is imprinted on the input basis, where the phase is no longer a complex function of coordinates  $x$  and  $y$ , but an operator acting on the input basis as a result of its composition in the coordinate operators  $x$  and  $y$ . Second, the reflected field, thus far expressed through coefficients in the input basis, is transferred to coefficients in the output basis through operator

$$U^{+\rightarrow-} = (U_G^{(+)} )^2 \exp\left(-2ik \frac{(x^{(+)} )^2 + (y^{(+)} )^2}{2R_u(z_A)}\right) \quad (16)$$

for mirror A and

$$U^{-\rightarrow+} = (U_G^{(-)} )^2 \exp\left(-2ik \frac{(x^{(-)} )^2 + (y^{(-)} )^2}{2R_u(z_B)}\right) \quad (17)$$

for mirror B, where  $R_u(z_A)$  and  $R_u(z_B)$  depend upon the chosen basis. This basis is most conveniently chosen so that the wavefront radius of curvature  $R_u(z_A)$  [ $R_u(z_B)$ ] matches the radius of curvature  $R_A$  ( $R_B$ ) of the quadratic component of the profile of mirror A (B). This choice uniquely specifies the basis and is assumed for the remainder of the paper. The mirror matrix A can then be expressed

$$A = (U_G^{(+)} )^2 \exp(-2ik \Delta_A^{(+)}), \quad (18)$$

where  $\Delta_A = f_A - (x^2 + y^2)/2R_A$  is the deviation of the profile of mirror A from the ideal parabolic surface.<sup>2</sup> If  $\Delta_A$  ( $\Delta_B$ ) can be evaluated as a matrix without taking integrals, the mirror matrix  $A$  ( $B$ ) can also be obtained without integrals, as discussed later in Sec. III E. We also note that, in the case of a small deviation  $\Delta_A$ , the mixing matrix elements can often be found through perturbation theory [45].

### C. Calculating polynomial mirror surface profiles

For the case where  $\Delta$  can be written as a power series in  $x$  and  $y$ , it is only necessary to calculate matrices of the various powers of  $x$  and  $y$  and sum each polynomial term with the appropriate coefficient. For the case of a parabolic distortion, the mirrors remain parabolic but with an adjusted radius of curvature, and therefore the cavity eigenmodes should match standard results. We have used this to test and validate our approach.

### D. Calculating the Gaussian surface profile

The Gaussian surface profile can also be expressed in the Hermite-Gaussian basis without taking integrals, but this requires a different approach, inspired by the Appendix of [50] and detailed in Appendix B. The matrix elements of a unit Gaussian profile with  $1/e$  waist  $w_e$  in a one-dimensional Hermite-Gaussian basis at axial coordinate  $z$  can be written

$$\begin{aligned} & \exp\left(-\frac{x^2}{w_e^2}\right)_{m',m}^{(\pm)}(z) \\ &= U_G^{(\pm)}(z)^\dagger (1 - \chi)^{-(m'+m+1)/2} \\ & \quad \times \left(\frac{\chi}{2}\right)^{(m'-m)/2} \sqrt{m'!m!} \\ & \quad \times \sum_{k=0}^{[m/2]} \frac{\binom{\chi^2}{4}^k}{\left(\frac{m'-m}{2} + k\right)!k!(m-2k)!} U_G^{(\pm)}(z), \end{aligned} \quad (19)$$

with

$$\chi = -\frac{1}{2} \frac{w(z)^2}{w_e^2}, \quad (20)$$

where  $m$  ( $m'$ ) is the index of the ingoing (outgoing) mode,  $(m' - m)/2$  is an integer, and  $m' \geq m$ . If  $(m' - m)/2$  is not an integer, the matrix element is zero. If  $m > m'$ , the symmetry  $\exp(-x^2/w_e^2)_{m',m} = \exp(-x^2/w_e^2)_{m,m'}$  should be used. The matrix  $U_G$  accounts for the Gouy phases of the basis states, as originally defined in Eq. (15). The two-dimensional profile is obtained from the one-dimensional matrices by a simple tensor product.

The deviation matrix  $\Delta$  of a Gaussian with depth  $D$  from the ideal parabolic surface is obtained from the matrix of the

unit profile through

$$\begin{aligned} \Delta^{(\pm)} = D \left[ 1 - \exp\left(-\frac{(x^{(\pm)})^2 + (y^{(\pm)})^2}{w_e^2}\right) \right] \\ - \frac{(x^{(\pm)})^2 + (y^{(\pm)})^2}{2R}, \end{aligned} \quad (21)$$

with

$$D = \frac{w_e^2}{2R}, \quad (22)$$

where  $R$  is the radius of curvature at the center of the Gaussian. The use of a single  $R$  in Eqs. (21) and (22) imposes that the wave-front radius of curvature of the basis states matches the mirror radius of curvature in the central depression.

### E. Taking the exponent of the surface profile

Once the surface profile deviation  $\Delta$  is expressed as a matrix, the surface profile phase matrix  $\exp(-2ik\Delta)$ , which constitutes the nontrivial component of the mirror matrix [Eq. (18)], can be calculated. It is tempting to calculate  $\exp(-2ik\Delta)$  through matrix exponentiation of  $-2ik\Delta$ , but this method cannot model losses; as  $\Delta$  is a Hermitian matrix, the matrix exponent is unitary and therefore every eigenvalue of a mirror matrix obtained through matrix exponentiation has unit modulus, meaning that the mirror is lossless. No matter how large a basis is chosen,  $\Delta$  never models processes representing transfer from inside to outside the basis and therefore no mechanism exists for power to leave the cavity.

To take the exponential in a way that can model losses, a procedure is used which is conceptually similar to the non-Hermitian Hamiltonian approach to simulating quantum systems that is commonly used in cavity quantum electrodynamics [51]. The matrix  $\Delta$  is first evaluated in a basis larger than the intended simulation basis, before being truncated to the size of the simulation basis according to specific rules: Each element of  $\Delta$  represents a transfer from an input state to an output state. If the input state lies within the simulation basis, but the output state is outside, that element encodes loss. Therefore, for each input state, the sum over all the magnitudes of transfers to states outside the basis is calculated, evaluating the amplitude leakage from the input basis state to outside the simulation basis. This summed rate is then added as a negative imaginary number onto the diagonal element of the input state. When the matrix exponential is then taken, this diagonal imaginary component causes loss rather than amplitude transfer.

Expressed mathematically, for a larger basis containing  $n_x$  and  $n_y$  up to maximum values of  $n_x^H$  and  $n_y^H$ , respectively, and the smaller simulation basis up to maximum values of  $n_x^{NH}$  and  $n_y^{NH}$ , respectively, components of the non-Hermitian  $\Delta$  matrix are written

$$\begin{aligned} \Delta_{n'_x, n'_y, n_x, n_y}^{(\pm)} &= \Delta_{n'_x, n'_y, n_x, n_y}^{H(\pm)}, \quad n'_x, n_x \leq n_x^{NH}, \quad n'_y, n_y \leq n_y^{NH}, \\ \delta_{n'_x, n_x} \delta_{n'_y, n_y} &= 0, \end{aligned} \quad (23a)$$

$$\begin{aligned} \Delta_{n_x, n_y, n_x, n_y}^{(\pm)} &= \Delta_{n_x, n_y, n_x, n_y}^{H(\pm)} + i \sum_{n'_x=(n_x^{NH}+1)}^{n_x^H} \sum_{n'_y=(n_y^{NH}+1)}^{n_y^H} \left| \Delta_{n'_x, n'_y, n_x, n_y}^{H(\pm)} \right|, \end{aligned} \quad (23b)$$

<sup>2</sup>In the paraxial approximation, the mathematically ideal mirror profile is parabolic. Outside this approximation, a spherical mirror is often a better match for the phase fronts [41].

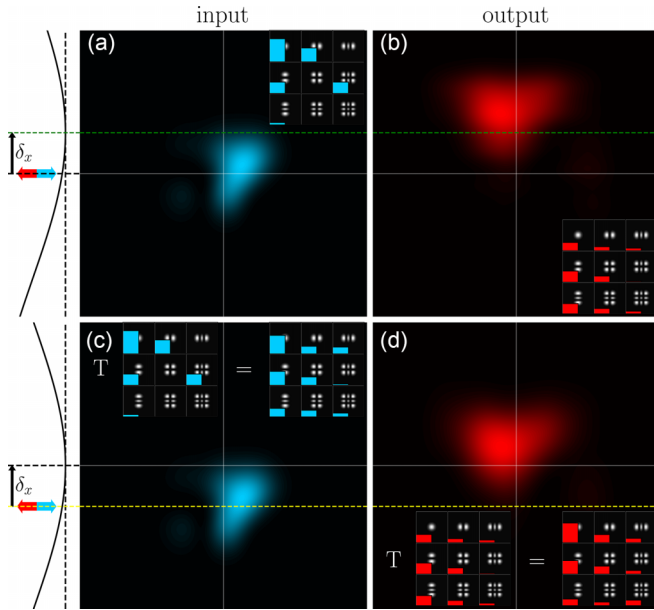


FIG. 4. Explanation of the method for obtaining the mirror matrix of a mirror translated in the  $x$  direction by  $\delta_x$ . (a) The input mode (blue) hits a translated mirror (black concave surface depicted on far left) and scatters to (b) the output mode (red). Both input and output modes are expressed as a linear superposition of basis states (here shown up to  $n_x$  and  $n_y$  of 2). (c) and (d) The same physical process described in a coordinate system centered on the mirror such that the mirror is nominally in the aligned configuration. Due to the shift in origin, the input and output fields have been translated using translation operator  $T$ . The physical equivalence of the two scenarios means that the action of the translated mirror can be derived from the untranslated mirror through suitable transformation of the input and output bases.

where  $\Delta^{H(\pm)}$  is the Hermitian surface profile deviation matrix evaluated on the larger basis. The matrix exponential of the non-Hermitian  $\Delta$  is then taken to find surface profile phase matrix  $\exp(-2ik\Delta)$ .

While this process is not mathematically identical to finding the true matrix  $\exp(-2ik\Delta)$ , in practice, this procedure produces almost identical loss results to numerical integration for most cavity configurations, as shown later in Sec. IV.

### F. Translating the mirror

With the surface profile phase matrix calculated, it is possible to evaluate both mirror matrices and thus obtain the eigenmodes for a cavity. To investigate the impact of transverse misalignment between the mirrors, the mirror matrices could be calculated for every misalignment separately. An alternative, discussed in this section, is to evaluate the mirror matrix in one transverse position (most conveniently the aligned configuration where any symmetries of the mirror profile can be exploited) and use translation operators to model transverse misalignment without calculating any further mirror matrix elements directly.

As depicted in Fig. 4, the action on a given input field of a mirror translated by  $\delta_x$  in the  $x$  direction is equivalent to the action of the untranslated mirror on the same input

field displaced by  $-\delta_x$ , because these two cases describe the same physical situation for different choices of origin. This equivalence means that the matrix of the translated mirror can be calculated by taking the matrix of the untranslated mirror and translating the input and output bases in the compensating direction.

The one-dimensional operator that translates the input and output bases is

$$T(\delta) = \exp\left(\delta \frac{\partial}{\partial x}\right), \quad (24)$$

with elements

$$T(\delta)_{m',m} = \sqrt{\frac{m!}{m'!}} \alpha^{m'-m} e^{-\alpha^2/2} L_n^{m'-m}(\alpha^2), \quad m' \geq m, \quad (25a)$$

$$T(\delta)_{m',m} = \sqrt{\frac{m'!}{m!}} (-\alpha^{m-m'}) e^{-\alpha^2/2} L_m^{m-m'}(\alpha^2), \quad m > m', \quad (25b)$$

where

$$\alpha = \frac{\delta}{w_0}, \quad (26)$$

$m$  ( $m'$ ) is the input (output) index in the one-dimensional basis, and  $\delta$  is the translation effected by the operator. This operator is identical to the displacement operator of the simple harmonic oscillator [52], owing to the close similarity between the simple-harmonic and Hermite-Gaussian bases. As the translation operator has the same elements in the input and output bases, translating a mirror with matrix  $C$  by  $\delta_x$  can be achieved through

$$C \rightarrow T_x^\dagger(-\delta_x) C T_x(-\delta_x), \quad (27)$$

where  $T_x$  is formed from the tensor product of the one-dimensional translation in the  $x$  direction and the identity in the  $y$  direction. If scanning the misalignment of the mirrors, the translation matrix need only be calculated for a single increment and then successively applied to generate all of the mirror matrices. In this way, the mirror profile and translation step matrices both need only be calculated once.

### G. Mode transformations

In addition to the  $x$ -translation operator  $T_x$  discussed in the preceding section, further transformation operators can be specified. Here we present transformation operators to change the central waist of a mode and to change its propagation angle. In the context of the present work, these operators are used not to calculate the cavity eigenmodes, but to evaluate geometric properties of these eigenmodes, as will be discussed in Sec. IV.

For the purposes of mode transformations, it is important to emphasize that, while the basis states [Eq. (10)] are running waves, the cavity field itself will be a standing wave. Solving for the cavity eigenmodes does not return the standing wave, but rather the running wave that reflects within the resonator to form the standing wave [the convention followed in Eq. (12) uses forward-propagating running waves]. This means that the transformations we described in this section act upon superpositions of running-wave basis states, not standing-wave fields.

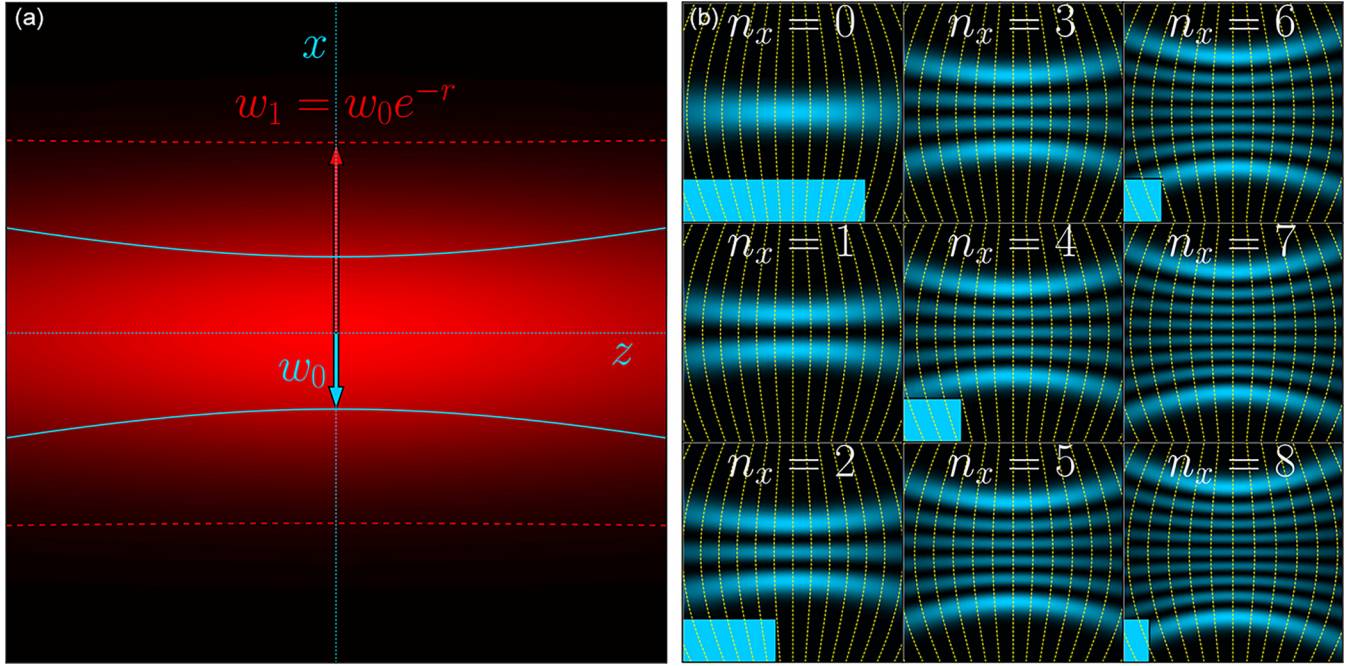


FIG. 5. Illustration of changing the waist of a mode through matrix methods, showing the modes in the  $xz$  plane. (a) A mode with waist  $w_1$  in the  $x$  direction, depicted through its intensity (red, gradient plot) and  $1/e$  waist (thick red dashed line), is expressed in the basis of modes with waist  $w_0$  in the  $x$  direction, indicated through its  $1/e$  waist (thick blue solid line). (b) Amplitude of the coefficients of the expanded mode with waist  $w_1$  [red intensity plot and thick dashed line in (a)] in the basis with waist  $w_0$ , where the label indicates the  $n_x$  index of the mode, the image the intensity profile in the  $xz$  plane, and the bar the amplitude of the mode in the superposition. The yellow dashed lines indicate the surfaces on which the electric field of the basis state has the same phase as the central plane. The radius of curvature of these surfaces corresponds to  $R_u$  of Eq. (10). The Gouy phase is responsible for the subtle spreading out of these surfaces as the basis state index increases. The rescaled fundamental mode is a linear superposition of even orders in the original basis. For simplicity, only the amplitudes of the state coefficients are plotted; however, it should be noted that both the phase of the coefficients and the relative Gouy phases of the basis states are crucial for determining the intensity profile of the mode.

The running-wave superpositions will nevertheless be referred to as modes as they directly correspond to standing-wave cavity modes.

### 1. Changing the mode waist

To scale the mode waist, we use the property that the Hermite-Gaussian basis states have the same functional form as the simple-harmonic-oscillator wave functions at the axial center of the mode ( $z = 0$ ). Therefore, the operator that changes the central waist of the mode is the same as the operator that rescales the coordinate operators of the simple harmonic oscillator, namely, the standard squeeze operators. The operator that changes the waist in the  $x$  direction from  $w_0$  to  $w_1$  is

$$S_x\left(\frac{w_1}{w_0}\right) = \exp\left\{-\frac{1}{2}r\left[a_x^2 - (a_x^\dagger)^2\right]\right\}, \quad (28a)$$

$$r = -\log\left(\frac{w_1}{w_0}\right). \quad (28b)$$

The use of this operator to expand the waist of a fundamental mode is depicted in Fig. 5. The same form of operator applies in the  $y$  direction for creation (annihilation) operator  $a_y^\dagger$  ( $a_y$ ). A similar form for this operator was also specified in [53], which uses a different formalism to apply operators to Gaussian modes.

### 2. Changing the mode angle

Finding the transformation operator to rotate the direction of propagation of the field is considerably more involved. This is because rotating an optical field  $\mathbf{E}(x, y, z, t)$  is not equivalent to rotating all of the basis states  $\{u_{nm}(x, y, z)\}$  due to two main complications. First, as the mode envelope is rotated, the implicit axial phase  $\exp(\mp ikz)$  must rotate with it. This “hidden” component will turn out to be the quantitatively dominant component of the rotation matrix. Second, while the optical field is a vector quantity, mode mixing is a scalar theory, with the polarization  $\epsilon$  factoring out. The rotation operator in the mode-mixing formalism rotates only the scalar field, whereas in a vector theory the rotation operator would also rotate the direction of the vector field.

With those complications noted, the operator to rotate the propagation direction can be derived. We consider an optical field  $\mathbf{E}(x, y, z, t)$ , which is a function of coordinates  $x$ ,  $y$ , and  $z$ . Next we define a new Cartesian coordinate system in which the axes have been rotated about the  $y$  axis to yield

$$\begin{aligned} x' &= x \cos(\phi_x) + z \sin(\phi_x), & y' &= y, \\ z' &= z \cos(\phi_x) - x \sin(\phi_x). \end{aligned} \quad (29)$$

The same optical field can be expressed in the new coordinate system through the function  $\mathbf{E}'(x', y', z', t)$ . The function  $\mathbf{E}'$  encodes the same field as  $\mathbf{E}$ , but, in its basis, the propagation direction is rotated towards the  $x'$  axis in the  $x'-z'$

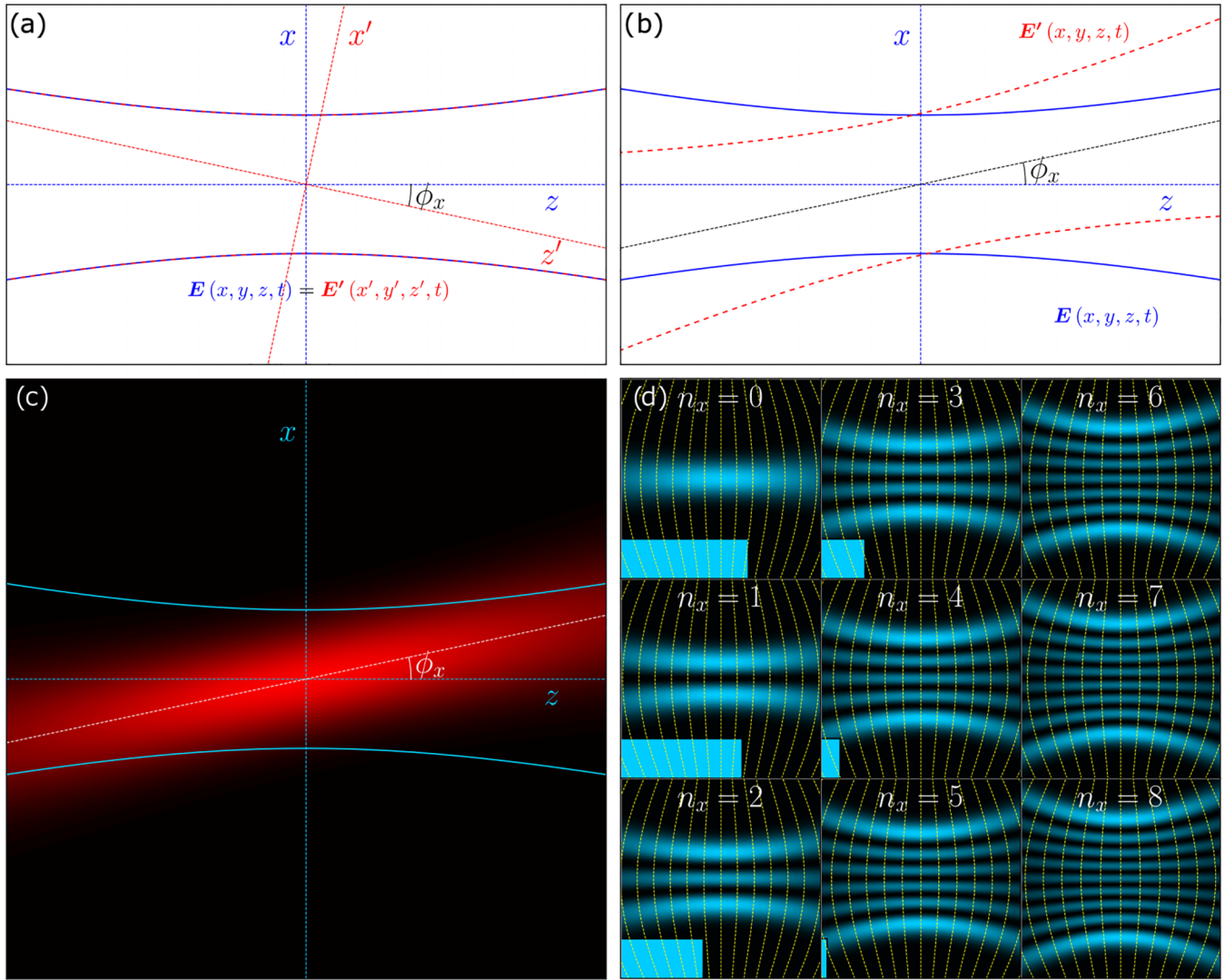


FIG. 6. Geometry used to derive the  $xz$  rotation operator and an example of its application to rotate the propagation direction of a fundamental mode. (a) A single field is described by two functions:  $\mathbf{E}(x, y, z, t)$  in coordinates  $x, y, z$ , and  $t$  and  $\mathbf{E}'(x', y', z', t)$  in coordinates  $x', y', z'$ , and  $t$ , where the primed coordinate system has been rotated by  $-\phi_x$  in the  $xz$  plane. The fields are depicted through their  $1/e$  waists, the thick blue solid lines and thick red dashed lines for  $\mathbf{E}$  and  $\mathbf{E}'$ , respectively, which overlap. (b) If the coordinate arguments of both functions are the same,  $\mathbf{E}'(x, y, z, t)$  (red dashed  $1/e$  waist) describes the same beam as  $\mathbf{E}(x, y, z, t)$  (blue solid  $1/e$  waist) but with the application of a rotation by  $\phi_x$  in the  $xz$  plane. (c) A fundamental mode with propagation angle  $\phi_x$  (red intensity plot) is expressed in the basis of modes propagating along the  $z$  axis with  $\phi_x = 0$  (blue solid lines indicating the  $1/e$  waist). (d) Amplitude of the coefficients of the rotated mode in the  $\phi_x = 0$  basis for  $n_x \in [0, 8]$ , where the image depicts the intensity profile of the basis states in the  $xz$  plane and the bar the amplitude of the basis state in the superposition. The yellow dashed lines indicate the surfaces on which the electric field of the basis state has the same phase as the central plane. As for Fig. 5, the phase of the basis state coefficients and the Gouy phases of the basis states contribute to the mode intensity in (c).

plane. Therefore, the transformation that takes the function  $\mathbf{E}$  to  $\mathbf{E}'$  is the operator for the propagation direction rotation, provided the coordinate arguments to both functions are the same. The coordinate systems used to derive the propagation direction-rotation operator, as well as the application of this operator to rotate the propagation direction of a mode, are depicted in Fig. 6.

The equivalence of  $\mathbf{E}$  and  $\mathbf{E}'$  in real space means that

$$\mathbf{E}'(x', y', z', t) = \mathbf{E}(x, y, z, t). \quad (30)$$

Now we assume that the rotation angle is small and thus denoted by  $\delta\phi_x$ . As, in the conventions of this paper, the mode

coefficients are not functions of the axial coordinate, any axial coordinate  $z'$  could be chosen, but for algebraic convenience we choose the  $z' = 0$  plane. A first-order approximation yields

$$\begin{aligned} x &= x', \quad y = y', \quad z = x' \delta\phi_x, \\ \mathbf{E}'(x', y', z' = 0, t) &= \mathbf{E}(x = x', y = y', z = x' \delta\phi_x, t). \end{aligned} \quad (31)$$

Recalling that the electric field  $\mathbf{E}$  is described by mode function  $u^{(\pm)}$  through Eq. (7) (and equivalently for  $\mathbf{E}'$  and  $u'^{(\pm)}$ ),

$$\begin{aligned} u'^{(\pm)}(x', y', z' = 0) &= u^{(\pm)}(x = x', y = y', z = x' \delta\phi_x) \\ &\times \exp[\mp ik(z = x' \delta\phi_x)]. \end{aligned} \quad (32)$$

Using the first-order expansions in  $\delta\phi_x$ , we obtain

$$u'^{(\pm)}(x, y, 0) = \left[ 1 + x\delta\phi_x \left( \mp ik + \frac{\partial}{\partial z} \right) \right] u^{(\pm)}(x, y, 0), \quad (33)$$

where  $x' = x$  and  $y' = y$  have been used to unify the function arguments. This therefore expresses the transformation of the basis functions associated with infinitesimal rotation of the electric field.

$$P_{xz}^{(\pm)}(\phi_x) = \exp \left\{ \mp i\phi_x \frac{kw_0}{2} \left[ (a_x + a_x^\dagger) \left( 1 + \frac{1}{(kw_0)^2} [(a_x - a_x^\dagger)^2 + (a_y - a_y^\dagger)^2] \right) \right] \right\}, \quad (34)$$

where the exponential is evaluated using the methods introduced in Sec. III E. Extending this form to more general changes to the propagation direction requires care, but, for the purposes of the analysis in this paper, the direction of transverse misalignment defines the  $x$  axis and therefore the propagation direction must lie in the  $xz$  plane.

#### H. Calculating mode angles

Finally, before effecting the mode rotations of Sec. III G 2, it is often useful to determine the propagation angle of the mode, which can be determined by calculating the expectation value of the angle operator

$$\phi_x^{(\pm)} = (\mp i/k) \frac{\partial}{\partial x} \quad (35a)$$

$$= (\mp i/(kw_0))(a_x - a_x^\dagger), \quad (35b)$$

which is valid in the paraxial approximation. The eigenstates of this operator are plane waves propagating at angle  $\phi_x$  to the  $z$  axis in the  $xz$  plane. This capability is useful to understand properties of resonant modes for misaligned cavity configurations.

### IV. DEMONSTRATING THE METHOD

#### A. Selecting the mode of interest

The mode-mixing method produces a set of cavity eigenmodes  $\{|\Psi_i\rangle\}$  and corresponding eigenvalues  $\{\gamma_i\}$ . The important data within these sets are the mode profile and round-trip loss of the particular eigenmode that will be used in the application at hand, and therefore a mode of interest should be identified. For the majority of applications using spherical cavities, the fundamental mode is more useful than the higher-order transverse modes. When the cavity mirrors are transversely misaligned or nonspherical, we expect the propagation angle and central waist of the fundamental mode to change (see Sec. II). Therefore, for this investigation, the eigenmode chosen is the  $|\Psi_i\rangle$  that maximizes the overlap  $|\langle\Psi_i|\Psi_{0,0}^G\rangle|^2$  with the geometrically expected mode denoted by  $|\Psi_{0,0}^G\rangle$ .

The geometric expectation  $|\Psi_{0,0}^G\rangle$  has thus far been parametrized through the propagation direction and the central waists in two principal directions, whereas the cavity eigenmodes  $\{|\Psi_i\rangle\}$  are expressed as coefficients in a basis propagating along the  $z$  axis. To find the overlap of the cavity

For finite rotations, the infinitesimal operator can be applied successively, and existing results can make the final form more useful. First, the  $x$  operator in the  $z = 0$  plane is  $x|_{z=0} = (kw_0/2)(a_x + a_x^\dagger)$  [see Eq. (15)]. Second, the basis functions satisfy the paraxial equation (8), and substituting the transverse derivative operators from Eq. (15) leads to the  $xz$  propagation direction operator

eigenmodes with the expected mode, the cavity eigenmodes were expressed in the same basis as the expected mode by first expanding or contracting in the two transverse directions independently to set the waists and then rotating the mode in the  $xz$  plane to set the propagation direction, according to the methods of Sec. III G.

#### B. Comparing to standard methods

Results obtained using the procedure for constructing mirror matrices using operators (presented in Sec. III) were compared with those found in the literature for the case of a Gaussian-shaped mirror [Figs. 7(a)–7(d)]. The round-trip loss was calculated as a function of cavity length for three different Gaussian waist values using both methods. Due to the different calculation bases employed by the methods, the results are not expected to be identical, but should agree up to convergence effects. As shown in Figs. 7(e) and 7(f) for the vast majority of cases, the methods predict round-trip losses with a fractional difference between one-hundredth and unity, discrepancies that are practically indiscernible amidst order of magnitude variations described in the data. The exceptions to this are highly concentric configurations, where there is a substantial difference between the losses predicted.

The methods presented for translating the mirror matrices (Sec. III F) enable the data generated for aligned configurations to be simply extended to misaligned configurations [Figs. 7(g)–7(i)]. This capability allows for the round-trip loss of cavities with transverse misalignment to be properly simulated, unveiling a rich structure of lossy bands in the length-misalignment parameter space that split into multiplets as the misalignment increases. Many of these bands can be traced back to loss peaks in the length scan of the aligned configuration, but some [such as the high loss bands in Fig. 7(h) appearing to originate from small misalignment at  $L/R = 1.5 \mu\text{m}$  for  $D = 5 \mu\text{m}$ ] cannot. This implies that residual misalignment introduces mechanisms of loss that do not feature for perfectly aligned cavities. A detailed discussion of the mode-mixing physics evident in Fig. 7 has been presented elsewhere [19].

### V. CONCLUSION

We have developed methods to calculate the modes of cavities with nonspherical and transversely misaligned mirrors.

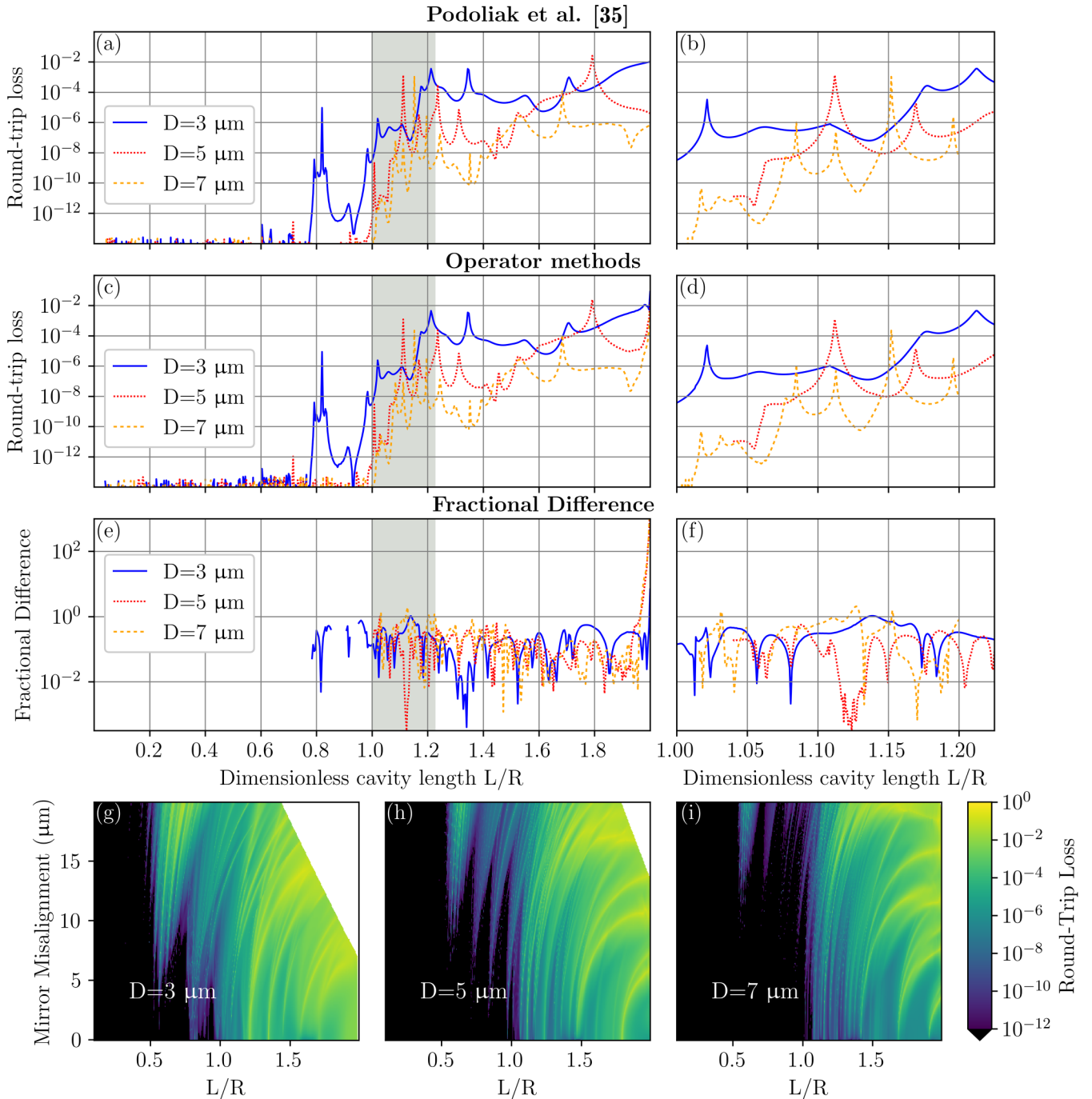


FIG. 7. Comparison of round-trip loss data for cavities with Gaussian mirrors generated with (a) and (b) standard methods and (c)–(f) methods described in this paper. All mirrors have a central radius of curvature of  $R_c = 500 \mu\text{m}$  and the interrogation wavelength is  $866 \text{ nm}$ . (a) Round-trip loss data generated using standard techniques for cavities with Gaussian mirrors of three depths as a function of cavity length over the whole stability region and (b) in a small region of lengths to the concentric side of the confocal length. Data were taken from [34]. The basis used was a Laguerre-Gaussian basis up to  $n = 30$ . (c) and (d) Equivalent round-trip loss data generated using the methods detailed in this paper, using a basis of the first 30 even states in both Cartesian directions. (e) and (f) Difference of the round-trip loss predicted by the two methods, expressed as a fraction of the loss predicted by the standard literature method of (a) and (b). Data are not shown where the literature round-trip loss is below  $10^{-12}$ . (g)–(i) Round-trip loss as a function of length and misalignment for the three mirrors using the translation methods described in Sec. III F. Configurations where the region inside one waist of the expected mode (as predicted by the theory of Sec. II) would not be fully enclosed within the concave region of the Gaussian mirror are left white. Below round-trip losses of  $10^{-12}$ , numerical noise becomes significant, and thus these results are left black.

We used a classical ray model to predict the mode axis and central waist of the resonant mode of a misaligned cavity, using these results to understand the output of a more complete mode-mixing method. This method is inspired by existing techniques that exploit well-known operator forms and transformation matrices to model mode mixing in cavities with different mirror profiles and to simply extend these models to include mirror misalignment.

The theory introduced in this paper is applicable to a variety of mode-mixing scenarios. First, for particular mirror shapes where the deviation from the ideal parabolic profile can be expressed as a sum of polynomials in the transverse coordinates, or as a Gaussian function, the mode-mixing matrix is calculated using analytical results and a matrix exponential, removing the need for any overlap integrals of the basis functions with the mirror profile to be taken. Second, once the mirror matrix has been obtained, the mirror can be translated using operators (which also do not require integrals to be calculated). This allows for the cavity mode structure under transverse misalignment to be determined in a simple manner and, in our experience, more quickly than with conventional techniques.

We anticipate the methods developed in this work will find application in the simulation of optical resonators with non-spherical mirrors, particularly for cases where the transverse misalignment of the mirrors is not negligible. An analysis of cavities with Gaussian-shaped mirrors utilizing the methods of this work is presented in [19].

Data underlying the results presented in this paper are available in Ref. [54]. The code that generated the data may be obtained from the authors upon reasonable request.

## ACKNOWLEDGMENTS

This work was funded by the UK Engineering and Physical Sciences Research Council Hub in Quantum Computing and Simulation (Grant No. EP/T001062/1) and the European Union Quantum Technology Flagship project AQTION (Project No. 820495). The authors would like to acknowledge the use of the University of Oxford Advanced Research Computing (ARC) facility in carrying out this work Ref. [55].

## APPENDIX A: DERIVATION OF OPERATORS IN THE HERMITE GAUSS BASIS

To derive the operator forms of  $x$  and  $\frac{\partial}{\partial x}$ , we start by comparing the mode amplitude of the basis states introduced in Eq. (10),

$$\begin{aligned} u_{n_x, n_y}^{(\pm)}(x, y, z) &= a(z) H_{n_x} \left( \frac{\sqrt{2}x}{w(z)} \right) H_{n_y} \left( \frac{\sqrt{2}y}{w(z)} \right) \\ &\times \exp \left( -\frac{x^2 + y^2}{w(z)^2} \right) \exp \left( \mp i k \frac{x^2 + y^2}{2R_u(z)} \right) \\ &\times \exp[\pm i(n_x + n_y + 1)\Psi_G], \end{aligned} \quad (\text{A1})$$

with the mode of the quantum harmonic oscillator of mass  $m$  and resonant frequency  $\Omega$ ,

$$\begin{aligned} \psi_{n_x, n_y}^{\text{HO}}(x, y) &= H_{n_x} \left( \sqrt{\frac{m\Omega}{\hbar}} x \right) H_{n_y} \left( \sqrt{\frac{m\Omega}{\hbar}} y \right) \\ &\times \exp \left( -\frac{m\Omega(x^2 + y^2)}{2\hbar} \right). \end{aligned} \quad (\text{A2})$$

The quantum harmonic oscillator has operators

$$x^{\text{HO}} = \sqrt{\frac{\hbar}{2m\Omega}} [a_x^{\text{HO}} + (a_x^{\text{HO}})^\dagger], \quad (\text{A3a})$$

$$\left( \frac{\partial}{\partial x} \right)^{\text{HO}} = \sqrt{\frac{m\Omega}{2\hbar}} [a_x^{\text{HO}} - (a_x^{\text{HO}})^\dagger], \quad (\text{A3b})$$

shown in terms of the harmonic annihilation operator  $a_x^{\text{HO}}$  [56]. In the case that the parameters of the harmonic oscillator and Gaussian mode are related by  $m\Omega/2\hbar = 1/w^2$ , the respective wave functions are related by

$$\begin{aligned} u_{n_x, n_y}^{\pm}(x, y) &= \psi(x, y)_{n_x, n_y}^{\text{HO}} \exp \left( \mp i k \frac{x^2 + y^2}{2R} \right) \\ &\times \exp[\pm i(n_x + n_y + 1)\Psi_G]. \end{aligned} \quad (\text{A4})$$

Therefore, the  $x$  operator in the cavity mode basis set can be found in terms of the  $x$  operator in the harmonic-oscillator basis

$$x_{n'_x, n'_y, n_x, n_y}^{(\pm)} = \int_S u_{n'_x, n'_y}^{\pm*}(x, y) x u_{n_x, n_y}^{\pm}(x, y) dx dy, \quad (\text{A5a})$$

$$\begin{aligned} x_{n'_x, n'_y, n_x, n_y}^{(\pm)} &= \exp[\pm i\Psi_G(n_x + n_y - n'_x - n'_y)] \\ &\times \int_S \psi_{n'_x, n'_y}^{*\text{HO}}(x, y) x \psi_{n_x, n_y}^{\text{HO}}(x, y) dx dy, \end{aligned} \quad (\text{A5b})$$

$$x_{n'_x, n'_y, n_x, n_y}^{(\pm)} = x_{n'_x, n'_y, n_x, n_y}^{\text{HO}} \exp[\pm i\Psi_G(n_x + n_y - n'_x - n'_y)]. \quad (\text{A5c})$$

The analogy between the wave functions then leads to

$$x^{(\pm)} = (U_G^{(\pm)})^\dagger \frac{1}{2} w (a_x + a_x^\dagger) U_G^{(\pm)}, \quad (\text{A6a})$$

$$(U_G^{(\pm)})_{n'_x, n'_y, n_x, n_y} = \delta_{n'_x, n_x} \delta_{n'_y, n_y} \exp[\pm i\Psi_G(n_x + n_y + 1)], \quad (\text{A6b})$$

where  $a_x$  is the annihilation operator in the  $x$  direction for the mode functions  $u_{n_x, n_y}^{(\pm)}(x, y, z)$ , which acts equivalently to the  $a_x^{\text{HO}}$  operator on the harmonic-oscillator wave functions. A similar approach can be used for the  $\frac{\partial}{\partial x}$  operator

$$\frac{\partial}{\partial x}^{(\pm)} = \int_S u_{n'_x, n'_y}^{\pm*}(x, y) \frac{\partial}{\partial x} u_{n_x, n_y}^{\pm}(x, y) dx dy, \quad (\text{A7a})$$

$$\begin{aligned} \frac{\partial}{\partial x}^{(\pm)} &= \exp[i\Psi_G(n_x + n_y - n'_x - n'_y)] \\ &\times \int_S \left( \psi_{n'_x, n'_y}^{*\text{HO}}(x, y) \frac{\partial}{\partial x} \psi_{n_x, n_y}^{\text{HO}}(x, y) \right) \\ &+ \left[ \psi_{n'_x, n'_y}^{*\text{HO}}(x, y) \left( \mp i k \frac{x}{R} \right) \psi_{n_x, n_y}^{\text{HO}}(x, y) \right] dx dy, \end{aligned} \quad (\text{A7b})$$

$$\frac{\partial}{\partial x}^{(\pm)} = (U_G^{(\pm)})^\dagger \left( \frac{\partial}{\partial x}^{\text{HO}} \mp \frac{ik}{R} x^{\text{HO}} \right) U_G^{(\pm)}, \quad (\text{A7c})$$

resulting in the expression

$$\frac{\partial}{\partial x} = (U_G^{(\pm)})^\dagger \left( \frac{1}{w} (a_x - a_x^\dagger) \mp i \frac{wk}{2R} (a_x + a_x^\dagger) \right) U_G^{(\pm)}, \quad (\text{A8})$$

which can be converted algebraically to the more convenient form

$$\frac{\partial}{\partial x} = \left( \frac{1}{w_0} (a_x - a_x^\dagger) \right). \quad (\text{A9})$$

## APPENDIX B: FINDING THE GAUSSIAN PROFILE MATRIX

The formula for the Gaussian profile surface matrix in the Hermite-Gaussian basis [Eq. (19)] is calculated following the method of Appendix A of [50]. To evaluate a unit-depth one-dimensional Gaussian as a matrix, we start by expanding using the transverse coordinate operator of Eq. (15),

$$\exp\left(-\frac{x^2}{w_e^2}\right) = (U_G^{(\pm)})^\dagger \exp\left\{\chi \left[ \frac{1}{2} (a^\dagger)^2 + \frac{1}{2} (a^\dagger)^2 + \frac{1}{2} (aa^\dagger + a^\dagger a) \right]\right\} U_G^{(\pm)} \quad (\text{B1a})$$

$$= (U_G^{(\pm)})^\dagger \exp[\chi(K_+ + K_- + 2K_0)] U_G^{(\pm)}, \quad (\text{B1b})$$

$$\chi = -\frac{w^2}{2w_e^2}, \quad (\text{B1c})$$

where  $K_+$ ,  $K_-$ , and  $K_0$  are  $\frac{1}{2}(a^\dagger)^2$ ,  $\frac{1}{4}(a^\dagger)^2$ , and  $\frac{1}{2}(aa^\dagger + a^\dagger a)$ , respectively, and the annihilation operator  $a$  represents  $a_x$  ( $a_y$ ) for the  $x$ - ( $y$ -)directed Gaussian function. Now use that  $K_+$ ,  $K_-$ , and  $K_0$  have the same commutation relations as  $-\sigma_+$ ,  $\sigma_-$ , and  $\frac{1}{2}\sigma_3$ , where

$$-\sigma_+ = \begin{pmatrix} 0 & -1 \\ 0 & 0 \end{pmatrix}, \quad \sigma_- = \begin{pmatrix} 0 & 0 \\ 1 & 0 \end{pmatrix},$$

$$\frac{1}{2}\sigma_3 = \frac{1}{2} \begin{pmatrix} 1 & 0 \\ 0 & -1 \end{pmatrix}. \quad (\text{B2})$$

Next we equate the coefficients of the exponent and normal-ordered exponents of the two-dimensional matrices, where the normal form has coefficients  $\zeta$ ,  $\zeta'$ , and  $\eta$ ,

$$\begin{aligned} & \exp[\zeta(-\sigma_+)] \exp[-\eta(\sigma_3)] \exp[\zeta'(\sigma_-)] \\ & = \exp[\chi(-\sigma_+) + \chi(\sigma_-) + 2\chi(\sigma_3)]. \end{aligned} \quad (\text{B3})$$

Expanding the two sides of this equation gives

$$\zeta = \zeta' = \frac{\chi}{1-\chi}, \quad \eta = 2 \ln(1-\chi). \quad (\text{B4})$$

The two-dimensional matrices are substituted back for creation and annihilation operators to obtain

$$\begin{aligned} & \exp[\chi(K_+ + K_- + 2K_0)] \\ & = \exp\left(\frac{\chi}{1-\chi} \frac{1}{2} (a^\dagger)^2\right) \\ & \quad \times \exp\left(-2 \ln(1-\chi) \frac{1}{4} (aa^\dagger + a^\dagger a)\right) \\ & \quad \times \exp\left(\frac{\chi}{1-\chi} \frac{1}{2} (a)^2\right). \end{aligned} \quad (\text{B5})$$

The normal operator form can be evaluated simply in the Hermite-Gaussian basis to obtain the result quoted in Sec. III D:

$$\begin{aligned} & \exp\left(-\frac{x^2}{w_e^2}\right)_{m',m}^{(\pm)} \\ & = (U_G^{(\pm)})^\dagger (1-\chi)^{-[(m'+m+1)/2]} \left(\frac{\chi}{2}\right)^{(m'-m)/2} \sqrt{m'!m!} \\ & \quad \times \sum_{k=0}^{\lfloor m/2 \rfloor} \frac{\left(\frac{\chi^2}{4}\right)^k}{\left(\frac{m'-m}{2} + k\right)! k! (m-2k)!} U_G^{(\pm)}, \end{aligned} \quad (\text{B6a})$$

$$\chi = -\frac{1}{2} \frac{w(z)^2}{w_e^2}. \quad (\text{B6b})$$

- 
- [1] A. E. Siegman, *Lasers* (University Science Books, Melville, 1986).
- [2] S. Buckley, K. Rivoire, and J. Vučković, Engineered quantum dot single-photon sources, *Rep. Prog. Phys.* **75**, 126503 (2012).
- [3] L. C. Flatten, Z. He, D. M. Coles, A. A. P. Trichet, A. W. Powell, R. A. Taylor, J. H. Warner, and J. M. Smith, Room-temperature exciton-polaritons with two-dimensional WS<sub>2</sub>, *Sci. Rep.* **6**, 33134 (2016).
- [4] F. Li, Y. Li, Y. Cai, P. Li, H. Tang, and Y. Zhang, Tunable open-access microcavities for solid-state quantum photonics and polaritonics, *Adv. Quantum Technol.* **2**, 1900060 (2019).
- [5] D. Hunger, T. Steinmetz, Y. Colombe, C. Deutsch, T. W. Hänsch, and J. Reichel, A fiber Fabry-Perot cavity with high finesse, *New J. Phys.* **12**, 065038 (2010).
- [6] M. Trupke, E. A. Hinds, S. Eriksson, E. Curtis, Z. Moktadir, E. Kikharenka, and M. Kraft, Microfabricated high-finesse optical cavity with open access and small volume, *Appl. Phys. Lett.* **87**, 211106 (2005).
- [7] A. Muller, E. B. Flagg, J. R. Lawall, and G. S. Solomon, Ultrahigh-finesse, low-mode-volume Fabry-Perot microcavity, *Opt. Lett.* **35**, 2293 (2010).
- [8] M. Uphoff, M. Brekenfeld, G. Rempe, and S. Ritter, Frequency splitting of polarization eigenmodes in microscopic Fabry-Perot cavities, *New J. Phys.* **17**, 013053 (2015).
- [9] G. W. Biedermann, Jr., F. Benito, K. Fortier, D. Stick, T. Loyd, P. Schwindt, C. Nakakura, R. Jarecki, Jr., and M. Blain, Ultraslow microfabricated mirrors for quantum information, *Appl. Phys. Lett.* **97**, 181110 (2010).
- [10] M. Aspelmeyer, T. J. Kippenberg, and F. Marquardt, Cavity optomechanics, *Rev. Mod. Phys.* **86**, 1391 (2014).
- [11] D. Kleckner, W. Marshall, M. J. A. de Dood, K. N. Dinyari, B.-J. Pors, W. T. M. Irvine, and D. Bouwmeester, High finesse

- opto-mechanical cavity with a movable thirty-micron-size mirror, *Phys. Rev. Lett.* **96**, 173901 (2006).
- [12] D. V. Karpov, S. Kurdiymov, and P. Horak, Convolutional neural networks for mode on-demand high finesse optical resonator design, *Sci. Rep.* **13**, 15567 (2023).
- [13] B. T. Walker, B. J. Ash, A. A. P. Trichet, J. M. Smith, and R. A. Nyman, Bespoke mirror fabrication for quantum simulation with light in open-access microcavities, *Opt. Express* **29**, 10800 (2021).
- [14] M. Kuznetsov, M. Stern, and J. Coppeta, Single transverse mode optical resonators, *Opt. Express* **13**, 171 (2005).
- [15] F. Ferdous, A. A. Demchenko, S. P. Vyatchanin, A. B. Matsko, and L. Maleki, Microcavity morphology optimization, *Phys. Rev. A* **90**, 033826 (2014).
- [16] F. M. Buters, M. J. Weaver, H. J. Eerks, K. Heeck, S. de Man, and D. Bouwmeester, Optomechanics with a polarization nondegenerate cavity, *Phys. Rev. A* **94**, 063813 (2016).
- [17] S. Gao, J. A. Blackmore, W. J. Hughes, T. H. Doherty, and J. F. Goodwin, Optimization of scalable ion-cavity interfaces for quantum photonic networks, *Phys. Rev. Appl.* **19**, 014033 (2023).
- [18] D. Kleckner, W. T. M. Irvine, S. S. R. Oemrawsingh, and D. Bouwmeester, Diffraction-limited high-finesse optical cavities, *Phys. Rev. A* **81**, 043814 (2010).
- [19] W. J. Hughes, T. H. Doherty, J. A. Blackmore, P. Horak, and J. F. Goodwin, Mode mixing and losses in misaligned microcavities, *Opt. Express* **31**, 32619 (2023).
- [20] J. L. Blows and G. Forbes, Mode characteristics of twisted resonators composed of two cylindrical mirrors, *Opt. Express* **2**, 184 (1998).
- [21] S. J. M. Habraken and G. Nienhuis, Modes of a twisted optical cavity, *Phys. Rev. A* **75**, 033819 (2007).
- [22] A. Yariv, *Quantum Electronics* (Wiley, New York, 1991).
- [23] A. Fox and T. Li, Modes in a maser interferometer with curved and tilted mirrors, *Proc. IEEE* **51**, 80 (1963).
- [24] A. Fox and T. Li, Computation of optical resonator modes by the method of resonance excitation, *IEEE J. Quantum Electron.* **4**, 460 (1968).
- [25] A. A. Ciobanu, D. D. Brown, P. J. Veitch, and D. J. Ottaway, Modeling circulating cavity fields using the discrete linear canonical transform, *J. Opt. Soc. Am. A* **38**, 1293 (2021).
- [26] M. V. Poplavskiy, A. B. Matsko, H. Yamamoto, and S. P. Vyatchanin, On fundamental diffraction limitation of finesse of a Fabry–Perot cavity, *J. Opt.* **20**, 075609 (2018).
- [27] R. G. Beausoleil, E. K. Gustafson, M. M. Fejer, E. D’Ambrosio, W. Kells, and J. Camp, Model of thermal wave-front distortion in interferometric gravitational-wave detectors. I. Thermal focusing, *J. Opt. Soc. Am. B* **20**, 1247 (2003).
- [28] P. Del’Haye, A. Schliesser, O. Arcizet, T. Wilken, R. Holzwarth, and T. J. Kippenberg, Optical frequency comb generation from a monolithic microresonator, *Nature (London)* **450**, 1214 (2007).
- [29] M. Kues, C. Reimer, P. Roztocky, L. R. Cortés, S. Sciara, B. Wetzl, Y. Zhang, A. Cino, S. T. Chu, B. E. Little *et al.*, On-chip generation of high-dimensional entangled quantum states and their coherent control, *Nature (London)* **546**, 622 (2017).
- [30] X. Shen, H. Choi, D. Chen, W. Zhao, and A. M. Armani, Raman laser from an optical resonator with a grafted single-molecule monolayer, *Nat. Photon.* **14**, 95 (2020).
- [31] J. Benedikter, T. Hümmer, M. Mader, B. Schleder, J. Reichel, T. W. Hänsch, and D. Hunger, Transverse-mode coupling and diffraction loss in tunable Fabry–Pérot microcavities, *New J. Phys.* **17**, 053051 (2015).
- [32] J. Benedikter, T. Moosmayer, M. Mader, T. Hümmer, and D. Hunger, Transverse-mode coupling effects in scanning cavity microscopy, *New J. Phys.* **21**, 103029 (2019).
- [33] A. A. P. Trichet, P. R. Dolan, and J. M. Smith, Strong coupling between 0D and 2D modes in optical open microcavities, *J. Opt.* **20**, 035402 (2018).
- [34] N. Podoliak, H. Takahashi, M. Keller, and P. Horak, Harnessing the mode mixing in optical fiber-tip cavities, *J. Phys. B* **50**, 085503 (2017).
- [35] D. V. Karpov and P. Horak, Cavities with nonspherical mirrors for enhanced interaction between a quantum emitter and cavity photons, *Phys. Rev. A* **105**, 023515 (2022).
- [36] D. V. Karpov and P. Horak, Evolutionary algorithm to design high-cooperativity optical cavities, *New J. Phys.* **24**, 073028 (2022).
- [37] L. C. Flatten, A. A. P. Trichet, and J. M. Smith, Spectral engineering of coupled open-access microcavities, *Laser Photon. Rev.* **10**, 257 (2016).
- [38] N. Barré, M. Romanelli, M. Lebental, and M. Brunel, Waves and rays in plano-concave laser cavities: I. Geometric modes in the paraxial approximation, *Eur. J. Phys.* **38**, 034010 (2017).
- [39] M. Lax, W. H. Louisell, and W. B. McKnight, From Maxwell to paraxial wave optics, *Phys. Rev. A* **11**, 1365 (1975).
- [40] P. K. Yu and K. M. Luk, Field patterns and resonant frequencies of high-order modes in an open resonator (short papers), *IEEE Trans. Microw. Theory Tech.* **32**, 641 (1984).
- [41] H. Laabs and A. T. Friberg, Nonparaxial eigenmodes of stable resonators, *IEEE J. Quantum Electron.* **35**, 198 (1999).
- [42] C. H. Nguyen, A. N. Utama, N. Lewty, and C. Kurtsiefer, Operating a near-concentric cavity at the last stable resonance, *Phys. Rev. A* **98**, 063833 (2018).
- [43] D. H. Foster, A. K. Cook, and J. U. Nöckel, Degenerate perturbation theory describing the mixing of orbital angular momentum modes in Fabry-Perot cavity resonators, *Phys. Rev. A* **79**, 011803(R) (2009).
- [44] M. Zeppenfeld and P. Pinkse, Calculating the fine structure of a Fabry-Perot resonator using spheroidal wave functions, *Opt. Express* **18**, 9580 (2010).
- [45] M. P. van Exter, M. Wubs, E. Hissink, and C. Koks, Fine structure in Fabry-Perot microcavity spectra, *Phys. Rev. A* **106**, 013501 (2022).
- [46] C. Koks, F. B. Baalbergen, and M. P. van Exter, Observation of microcavity fine structure, *Phys. Rev. A* **105**, 063502 (2022).
- [47] D. Stoler, Operator methods in physical optics, *J. Opt. Soc. Am.* **71**, 334 (1981).
- [48] G. Nienhuis and L. Allen, Paraxial wave optics and harmonic oscillators, *Phys. Rev. A* **48**, 656 (1993).
- [49] M. Jaffe, L. Palm, C. Baum, L. Taneja, and J. Simon, Aberrated optical cavities, *Phys. Rev. A* **104**, 013524 (2021).
- [50] S. Varró, Coherent and incoherent superposition of transition matrix elements of the squeezing operator, *New J. Phys.* **24**, 053035 (2022).
- [51] A. Kuhn, in *Engineering the Atom-Photon Interaction: Controlling Fundamental Processes with Photons, Atoms and Solids*, edited by A. Predojević and M. W. Mitchell (Springer, Cham, 2015), pp. 3–38.

- [52] K. E. Cahill and R. J. Glauber, Ordered expansions in boson amplitude operators, *Phys. Rev.* **177**, 1857 (1969).
- [53] S. J. M. Habraken and G. Nienhuis, Geometric phases in astigmatic optical modes of arbitrary order, *J. Math. Phys.* **51**, 082702 (2010).
- [54] <https://doi.org/10.5258/SOTON/D2938>.
- [55] <http://dx.doi.org/10.5281/zenodo.22558>.
- [56] J. Schwinger, in *Quantum Mechanics: Symbolism of Atomic Measurements*, edited by B.-G. Englert (Springer, Berlin, 2001).